Ice loss from the East Antarctic Ice Sheet during late Pleistocene interglacials

David J. Wilson[1*], Rachel A. Bertram[1], Emma F. Needham[1], Tina van de Flierdt[1], Kevin J. Welsh[2], Robert M. McKay[3], Anannya Mazumder[2], Christina R. Riesselman[4], Francisco J. Jimenez-Espejo[5,6], Carlota Escutia[6]

[1]*Department of Earth Science and Engineering, Imperial College London, UK*

*(*david.wilson1@imperial.ac.uk)*

[2]*School of Earth and Environmental Sciences, University of Queensland, Australia*

[3]*Antarctic Research Centre, Victoria University of Wellington, New Zealand*

[4]*Department of Geology and Department of Marine Science, University of Otago, New Zealand*

[5]*Dept of Biogeochemistry, JAMSTEC, Japan*

[6]*IACT-CSIC and Universidad de Granada, Spain*

Understanding ice sheet behaviour in the geological past is essential for evaluating the role of the cryosphere in the climate system and for projecting rates and magnitudes of sea level rise in future warming scenarios[1-4]. While both geological data[5-7] and ice sheet models[3,8] indicate instability of marine-based sectors of the East Antarctic Ice Sheet during Pliocene warm intervals, the ice sheet dynamics during late Pleistocene interglacials are highly uncertain[3,9,10]. Here we provide evidence from marine sedimentological and geochemical records for ice margin retreat or thinning in the vicinity of the Wilkes Subglacial Basin of East Antarctica during warm late Pleistocene interglacials. The most extreme changes in sediment provenance, recording changes in the locus of glacial erosion, occurred during marine isotope stages 5, 9, and 11, when

Antarctic air temperatures[11] were at least 2 °C warmer than pre-industrial for 2500 years or more. Hence, our study indicates a close link between extended Antarctic warmth and ice loss from the Wilkes Subglacial Basin, providing the first ice-proximal data supporting a sea level contribution from a reduced East Antarctic Ice Sheet during warm interglacials. While the behaviour of other regions of the East Antarctic Ice Sheet remains to be assessed, it appears that modest future warming may be sufficient to cause ice loss from the Wilkes Subglacial Basin.

Ice sheet growth and decay act as major controls on regional and global climate by influencing albedo, sea ice extent, atmospheric and ocean circulation, nutrient supply, and sea level. In particular, the behaviour of the polar ice sheets is a key uncertainty in predicting sea level rise beyond the end of this century[1,2]. Complete melting of the marine-based West Antarctic Ice Sheet (WAIS) would contribute ~3-5 m to global mean sea level, while the East Antarctic Ice Sheet (EAIS) contains a sea level equivalent of ~53 m, of which ~19 m is also marine-based ice[12]. Although such ice is susceptible to loss through marine ice sheet instability processes where the bed deepens inland[13], modelling studies differ in their predictions for both past and future ice sheet stability[2-4,8-10,14]. It is therefore crucial to use geological evidence from proximal to ice sheet margins[5-7,15,16] in order to constrain ice sheet responses to climate forcing.

The late Pleistocene interval represents a critical target for exploring ice sheet behaviour because of similar ice sheet boundary conditions to the present day (cf. ref. 8) and well-constrained evidence on global mean sea levels[17] and regional climatic forcing[11,18,19]. Global mean sea levels were 6-9 m higher than present during interglacial marine isotope stage (MIS) 5e, and 6-13 m higher than present during interglacial MIS 11, probably requiring a significant ice reduction in Antarctica[17]. Sedimentological evidence suggests that the

Pleistocene ice sheets draining into the Ross Sea Embayment fluctuated on glacial-interglacial timescales[15], while collapse of the WAIS was proposed for at least one Pleistocene interglacial[16]. Although proximal marine sedimentary records indicate a dynamic margin for both the WAIS and the EAIS during warm Pliocene intervals[5-7,15], there are currently no data directly constraining EAIS behaviour during the late Pleistocene.

Here we provide the first observations constraining the behaviour of a marine-based sector of the EAIS during the late Pleistocene, based on sedimentological and geochemical records in marine sediment core U1361A (64.41°S, 143.89°E, 3454 m water depth), recovered from the continental rise offshore of the Wilkes Subglacial Basin (Fig. 1) during IODP Expedition 318 (ref. 20). Because of its landward-sloping bed and ~3-4 m sea level equivalent contained in marine-based ice (refs. 2,12), the Wilkes Subglacial Basin represents both a sensitive test for EAIS vulnerability[9] and a significant potential contributor to global sea level. Glacial-interglacial cycles are well resolved in the upper 7.5 metres of U1361A, with glacial intervals indicated by diatom-poor silty clays with occasional laminations and low barium/aluminium (Ba/Al) ratios, and interglacial intervals marked by bioturbated diatom-rich clays with high Ba/Al ratios, high sediment reflectance and occasional dropstones[20] (Fig. 2a-e). These lithological cycles record changes in local productivity, likely due to reduced presence of sea-ice during interglacials[20]. Assignment of the diatom-rich intervals to the past five interglacials (pink bars in Fig. 2) is well supported by all available chronostratigraphic datums (Methods; Extended Data Fig. 3; Table S8).

Since sediment supply to the continental rise at Site U1361 is dominated by downslope transport from the proximal shelf (ref. 20; Methods), sediment provenance in this location is sensitive to processes at the regional ice sheet margin. To constrain provenance changes through time, we analysed neodymium (Nd) isotopic compositions on the bulk sediment

fraction (Methods) at approximately 10 cm intervals (~6 kyr resolution). These data are expressed as ε_{Nd}, the deviation of $^{143}Nd/^{144}Nd$ ratios from the Chondritic Uniform Reservoir value in parts per 10,000. Since Nd isotopes vary as a function of the age and lithology of the eroded source rocks, they are an appropriate tracer for changes in the distribution of glacial erosion in the vicinity of the Wilkes Subglacial Basin[5]. Sediment grain size (% 250 μm – 2 mm) was also measured to provide complementary evidence on the supply of iceberg-rafted debris (IBRD) from calving ice margins (Methods).

Our detrital Nd isotope record reveals variability between ε_{Nd} = -15.5 to -12 during glacials and ε_{Nd} = -12 to -8.5 during interglacials (Fig. 2f), corresponding closely with sea-ice retreat and productivity changes inferred from Ba/Al ratios (Fig. 2e; Methods). Provenance shifts towards more radiogenic Nd isotopic compositions at the onset of interglacials MIS 5 and MIS 9 coincide closely with peaks in the supply of IBRD, whereas IBRD peaks slightly precede the provenance changes for MIS 7 and MIS 11 (Fig. 2f,g). While IBRD peaks are transient events recording dynamic ice discharge typically during deglaciation[6] (Methods), the provenance changes are sustained for longer and suggest a prolonged switch in the locus of regional glacial erosion. Additional minor IBRD peaks occur near the ends of diatom-rich intervals, potentially recording an advancing ice margin at the onset of glaciation.

The sediment provenance changes at U1361A during the late Pleistocene are strikingly similar in pattern and magnitude to changes reported previously for the Pliocene, which ranged from ε_{Nd} = -15 to -6 (ref. 5). Hence, we infer that similar lithologies were eroded during both periods, which is further supported by detrital strontium (Sr) isotope data (Extended Data Fig. 2). In detail, unradiogenic Nd isotopic compositions during late Pleistocene glacials (ε_{Nd} = -15.5 to -12) record a dominant Lower Paleozoic provenance (ε_{Nd} = -20 to -10), which is explained by bedrock erosion of Lower Paleozoic granitoids near the

modern ice margin, particularly around the Ninnis Glacier[5] (Extended Data Fig. 1). In contrast, the more radiogenic compositions during interglacials (up to ε_{Nd} values of -8.5) require additional contributions from a more radiogenic source that is inferred to be the Permian-Cretaceous rocks of the Ferrar Large Igneous Province (FLIP) (ε_{Nd} = -7 to -3.5; ref 5). Such FLIP basalts and dolerites, and associated Beacon Supergroup sediments, are not exposed in significant areas at the present ice margin, with only a small coastal outcrop at Horn Bluff (Extended Data Fig. 1), but are extensively present within the ice-covered Wilkes Subglacial Basin[5,21]. The admixture of a FLIP component within the interglacial sediments at U1361A is independently supported by acid-reductive leaching experiments, which extract a reactive component with a Nd isotopic composition consistent with the FLIP (Extended Data Fig. 1; Methods).

An enhanced contribution of FLIP lithologies to Site U1361 during warmer than present interglacials (Fig. 2f) must indicate a shift in the erosional regime of the ice sheet and/or a change in sediment transport to the site. Although the flow speed of the wind-driven westward-flowing Antarctic Coastal Current[22] could have changed through time, we argue against sediment transport changes as the dominant control on our provenance record. First, warming is proposed to weaken the polar easterlies and reduce the strength of the Antarctic Coastal Current[22,23], whereas an enhanced supply of FLIP-derived sediments from upstream coastal sources (e.g. Horn Bluff) during warm interglacials would instead require a strengthened current. Second, we observe similar Nd isotope values and temporal variability in the bulk and fine (< 63 μm) sediment fractions for 10 co-analysed samples in U1361A (Extended Data Fig. 1; Methods), which rules out mineralogical or grain size sorting as a major control on the record. Third, a record of sortable silt mean grain size in U1361A (Table S4) provides no evidence for significant deep flow speed changes, and shows no co-variation with detrital Nd isotopes, which is consistent with a turbidite-dominated transport

environment but inconsistent with deep current transport driving the radiogenic Nd isotope signal (Methods).

Because ice sheets predominantly erode bedrock near their margins[24], we consider past interglacial retreat of the ice margin into the Wilkes Subglacial Basin[2,3,9] (Fig. 1b), coupled to enhanced erosion of FLIP bedrock and/or FLIP-derived sediment infill of the Central Basin[21], as the most likely explanation for the provenance changes at Site U1361. Additionally, enhanced erosion of FLIP and associated Beacon lithologies close to the mouth of the Wilkes Subglacial Basin could possibly have contributed to the provenance shift. Without necessitating full-scale retreat, this latter scenario would require a significant change in the erosion distribution, implicating flow acceleration linked to ice sheet thinning[24]. While we cannot quantitatively determine the relative importance of margin retreat versus thinning, we emphasise that either scenario would imply a close link between detrital provenance and ice volume reduction in the Wilkes Subglacial Basin, and hence a late Pleistocene sea level contribution from the EAIS.

The key finding from our new dataset is that the Wilkes Subglacial Basin has been susceptible to ice loss not only during warm Pliocene intervals with CO_2 levels of ~400 ppm (ref. 5), but also during the late Pleistocene despite CO_2 levels remaining below 300 ppm (ref. 25). Hence, we provide the first data-based evidence in support of recent ice sheet models which simulate margin retreat and ice loss during late Pleistocene interglacials[2,3,9] (Fig. 1b). While global climate forcing during recent interglacials was generally similar to the Holocene, evidence from both Antarctica[11] and the Southern Ocean[18,19] reveals that a number of these interglacials were at times characterised by warmer temperatures than the Holocene (Fig. 3a-c), consistent with a link between regional warming and ice sheet retreat[2,3]. Possible causes of transient warmth include a bipolar seesaw tied to variability of the Atlantic

meridional overturning circulation[11], wind shifts that enhanced Circumpolar Deep Water upwelling onto the shelves[26], or feedbacks linked to the size of the WAIS (ref. 27).

In detail, it is striking that differences in Nd isotopic compositions between individual interglacials correlate well with Southern Ocean temperatures[11,18,19] (Fig. 3a-c) and global sea level[17,28] (Fig. 3f). In particular, MIS 5, 9 and 11, with the most distinct radiogenic Nd isotope excursions (Fig. 3e), experienced the most extended warmth in Antarctica[11] (Fig. 3a), with temperatures more than 2 °C warmer than the pre-industrial late Holocene for ~4 kyr, ~2.5 kyr and ~6 kyr respectively. In contrast, MIS 7 had a more muted Nd isotope response, comparable to the transition from the Last Glacial Maximum into the Holocene (Fig. 3e), and experienced temperatures more than 2 °C warmer than the pre-industrial late Holocene for only ~1 kyr (Fig. 3a). Such a scaling between the magnitude and duration of regional climate warming, the Nd isotope-based provenance variations, and global sea level (Fig. 3) is consistent with an ice volume change in the Wilkes Subglacial Basin. We therefore suggest that an Antarctic warming of ~2 °C above pre-industrial temperatures for ~1-2.5 kyr has been sufficient to cause ice loss beyond that of the modern day or pre-industrial Holocene, leading to a contribution to global sea levels from the EAIS during MIS 5, 9 and 11, in agreement with recent modelling results for MIS 5e (ref. 3).

Differences in provenance between individual interglacials (Fig. 3e) also hint at the underlying mechanisms of ice retreat in the Wilkes Subglacial Basin, by supporting variable ice margin retreat during climate warming, rather than a simple switch between advanced and retreated states[2] (Fig. 1b). Variable retreat could reflect the presence of multiple pinning points on basement highs[9,24] (Fig. 1b), which represent temporary or final limits for the ice margin. In this view, the more extreme radiogenic Nd isotope excursions observed during

some (but not all) warm Pliocene intervals[5] may indicate more substantial ice sheet retreat at these times.

Although we have focused on ice sheet behaviour during individual interglacials, our data also provide an indication of longer timescale changes in ice sheet dynamics. Over the last ~480 kyr, there is a long term trend towards declining IBRD (Fig. 2g), suggesting an increasingly stable ice margin, while glacial ε_{Nd} values have become less extreme (i.e. more radiogenic) (Fig. 2f), potentially indicating reduced glacial advance over the shelf. Together, these observations appear consistent with a gradual stabilisation of the ice margin as a consequence of grounding zone sediment accumulation through multiple glacial cycles[29,30], but this hypothesis awaits further testing.

By providing the first geological evidence for ice loss from a dynamic margin of the EAIS during recent warm interglacials (MIS 5, 9 and 11), our data place new constraints on the role of Antarctica in past sea level change, and represent a useful target for ice sheet models. Based on the ice sheet response during past interglacial periods, we estimate that significant ice loss within the Wilkes Subglacial Basin would likely occur with ~2 °C warming (above pre-industrial) if sustained for a few millennia. This scenario is broadly consistent with the magnitudes and timescales of forcing that generate ice margin retreat in models[2-4]. While evidence from sediment provenance cannot precisely quantify the magnitude of any sea level contribution, our data appears to suggest that some models (e.g. refs. 9,14) may have underestimated the long-term potential of the Wilkes Subglacial Basin, and perhaps the EAIS more generally, to contribute to future sea level rise.

References

1 IPCC. *Climate Change 2013: The Physical Science Basis. Contribution of Working Group I to the Fifth Assessment Report of the Intergovernmental Panel on Climate Change [Stocker, T.F., D. Qin, G.-K. Plattner, M. Tignor, S.K. Allen, J. Boschung, A. Nauels, Y. Xia, V. Bex and P.M. Midgley (eds.)]*. 1535 (Cambridge University Press, 2013).

2 Mengel, M. & Levermann, A. Ice plug prevents irreversible discharge from East Antarctica. *Nat. Clim. Chang.* **4**, 451-455 (2014).

3 DeConto, R. M. & Pollard, D. Contribution of Antarctica to past and future sea-level rise. *Nature* **531**, 591-597 (2016).

4 Golledge, N. R. *et al.* The multi-millennial Antarctic commitment to future sea-level rise. *Nature* **526**, 421-425 (2015).

5 Cook, C. P. *et al.* Dynamic behaviour of the East Antarctic ice sheet during Pliocene warmth. *Nat. Geosci.* **6**, 765-769 (2013).

6 Patterson, M. O. *et al.* Orbital forcing of the East Antarctic ice sheet during the Pliocene and Early Pleistocene. *Nat. Geosci.* **7**, 841-847 (2014).

7 Reinardy, B. T. I. *et al.* Repeated advance and retreat of the East Antarctic Ice Sheet on the continental shelf during the early Pliocene warm period. *Paleogeogr. Paleoclimatol. Paleoecol.* **422**, 65-84 (2015).

8 Austermann, J. *et al.* The impact of dynamic topography change on Antarctic ice sheet stability during the mid-Pliocene warm period. *Geology* **43**, 927-930 (2015).

9 Golledge, N. R., Levy, R. H., McKay, R. M. & Naish, T. R. East Antarctic ice sheet most vulnerable to Weddell Sea warming. *Geophys. Res. Lett.* **44**, 2343-2351 (2017).

10 Pollard, D. & DeConto, R. M. Modelling West Antarctic ice sheet growth and collapse through the past five million years. *Nature* **458**, 329-332 (2009).

11 Jouzel, J. *et al.* Orbital and millennial Antarctic climate variability over the past 800,000 years. *Science* **317**, 793-796 (2007).

12 Fretwell, P. *et al.* Bedmap2: improved ice bed, surface and thickness datasets for Antarctica. *Cryosphere* **7**, 375-393 (2013).

13 Schoof, C. Ice sheet grounding line dynamics: Steady states, stability, and hysteresis. *J. Geophys. Res.-Earth Surf.* **112**, doi: 10.1029/2006jf000664 (2007).

14 Ritz, C. *et al.* Potential sea-level rise from Antarctic ice-sheet instability constrained by observations. *Nature* **528**, 115-118 (2015).

15 Naish, T. *et al.* Obliquity-paced Pliocene West Antarctic ice sheet oscillations. *Nature* **458**, 322-328 (2009).

16 Scherer, R. P. *et al.* Pleistocene collapse of the West Antarctic ice sheet. *Science* **281**, 82-85 (1998).

17 Dutton, A. *et al.* Sea-level rise due to polar ice-sheet mass loss during past warm periods. *Science* **349**, aaa4019 (2015).

18 Elderfield, H. *et al.* Evolution of ocean temperature and ice volume through the Mid-Pleistocene Climate Transition. *Science* **337**, 704-709 (2012).

19 Martinez-Garcia, A. *et al.* Links between iron supply, marine productivity, sea surface temperature, and CO_2 over the last 1.1 Ma. *Paleoceanography* **24**, doi: 10.1029/2008pa001657 (2009).

20 Escutia, C., Brinkhuis, H., Klaus, A. & Scientists, E. *Proc. IODP, 318, Wilkes Land glacial history*. Vol. 318 (Integrated Ocean Drilling Program Management International, 2011).

21 Ferraccioli, F., Armadillo, E., Jordan, T., Bozzo, E. & Corr, H. Aeromagnetic exploration over the East Antarctic Ice Sheet: A new view of the Wilkes Subglacial Basin. *Tectonophysics* **478**, 62-77 (2009).

22 Spence, P. *et al.* Rapid subsurface warming and circulation changes of Antarctic coastal waters by poleward shifting winds. *Geophys. Res. Lett.* **41**, 4601-4610 (2014).

23 DeConto, R., Pollard, D. & Harwood, D. Sea ice feedback and Cenozoic evolution of Antarctic climate and ice sheets. *Paleoceanography* **22**, doi: 10.1029/2006pa001350 (2007).

24 Golledge, N. R. *et al.* Antarctic climate and ice-sheet configuration during the early Pliocene interglacial at 4.23 Ma. *Clim. Past.* **13**, 959-975 (2017).

25 Siegenthaler, U. *et al.* Stable carbon cycle-climate relationship during the late Pleistocene. *Science* **310**, 1313-1317 (2005).

26 Fogwill, C. J. *et al.* Testing the sensitivity of the East Antarctic Ice Sheet to Southern Ocean dynamics: past changes and future implications. *J. Quat. Sci.* **29**, 91-98 (2014).

27 Holden, P. B. *et al.* Interhemispheric coupling, the West Antarctic Ice Sheet and warm Antarctic interglacials. *Clim. Past.* **6**, 431-443 (2010).

28 Waelbroeck, C. *et al.* Sea-level and deep water temperature changes derived from benthic foraminifera isotopic records. *Quat. Sci. Rev.* **21**, 295-305 (2002).

29 Alley, R. B., Anandakrishnan, S., Dupont, T. K., Parizek, B. R. & Pollard, D. Effect of sedimentation on ice-sheet grounding-line stability. *Science* **315**, 1838-1841 (2007).

30 Pollard, D. & DeConto, R. M. A coupled ice-sheet/ice-shelf/sediment model applied to a marine-margin flowline: forced and unforced variations. *Glacial Sedimentary Processes and Products* 37-52 (2007).

Online Content Any Methods, including any statements of data availability and Nature Research reporting summaries, along with any additional references and Source Data files, are available in the online version of the paper.

Supplementary Information is available in the online version of the paper.

Acknowledgements This research used samples and data provided by the Integrated Ocean Drilling Program (IODP), which is sponsored by the US National Science Foundation (NSF) and participating countries under the management of Joint Oceanographic Institutions. D.J.W. thanks B. Coles, C. Huck, K. Kreissig, N. Pratt and P. Simoes Pereira for technical support. D.J.W., R.A.B., E.F.N. and T.v.d.F. acknowledge financial support from the Kristian Gerhard Jebsen Foundation, the Leverhulme Trust (RPG-398) and NERC (NE/N001141/1, NE/H025162/1). K.J.W. was funded by an Australian Research Council LIEF grant (LE140100047). R.M.M. was funded by a Royal Society (New Zealand) Rutherford Discovery Fellowship (RDF-13-VUW-003). C.E. and F.J.J.-E. acknowledge funding from the Spanish Ministry of Science and Innovation Grant CTM2014-60451-C2-1-P co-financed by the European Regional Development Fund (FEDER).

Author Contributions D.J.W., T.v.d.F., and K.J.W. designed the research; D.J.W., R.A.B., E.F.N., and T.v.d.F. carried out the Nd isotope analyses; R.A.B. carried out the Sr isotope analyses; A.M. performed the diatom counts with input from K.J.W. and C.R.R.; R.M.M. and K.J.W. carried out sedimentological analyses; F.J.J.-E. and C.E. conducted XRF scanning measurements and PCA analysis; C.R.R., K.J.W., and R.M.M. generated the age model. All authors contributed to data interpretation. D.J.W. wrote the paper, with input from all authors.

Data availability All data from this study can be found in the Supplementary Information.

Competing interests The authors declare no competing interests.

Reprints and permissions information is available at http://www.nature.com/reprints.

Correspondence and requests for materials should be addressed to D.J.W. (david.wilson1@imperial.ac.uk).

Figures

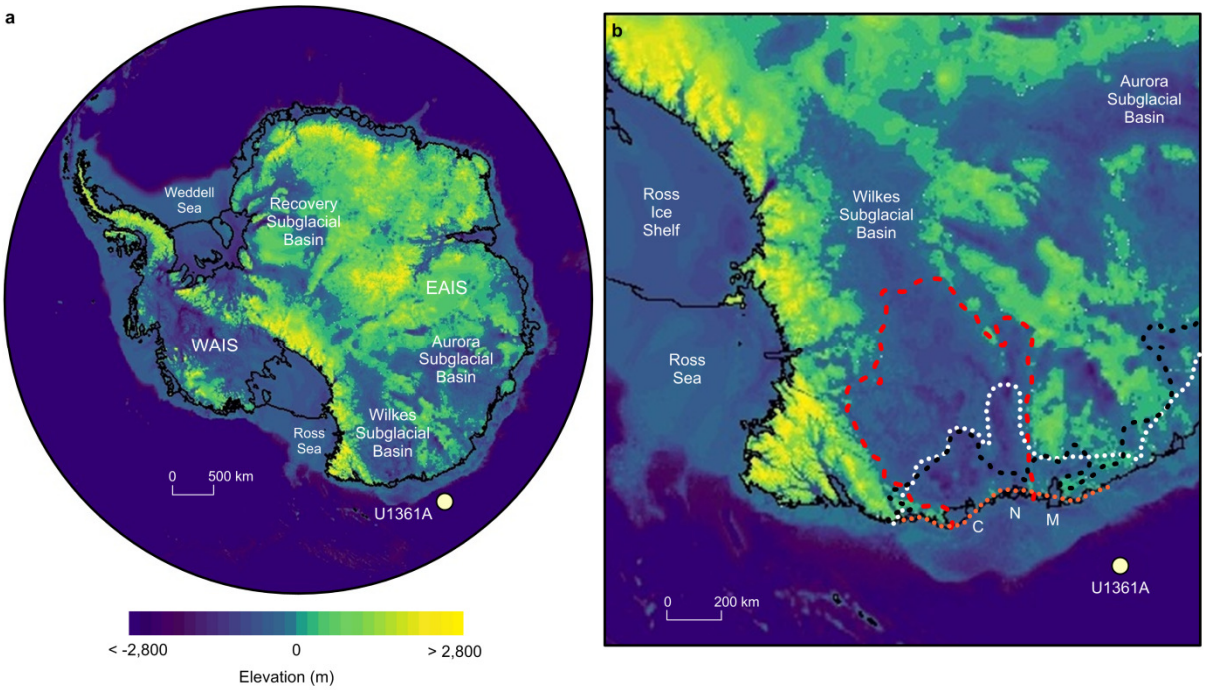

Figure 1: Setting of sediment core U1361A offshore of the Wilkes Subglacial Basin. (**a**) Map of Antarctica showing the subglacial bedrock elevation above sea level[12] and core U1361A location. EAIS, East Antarctic Ice Sheet; WAIS, West Antarctic Ice Sheet. (**b**) Detailed map of the Wilkes Subglacial Basin, with lines illustrating positions of the ice sheet margin in different ice sheet models and scenarios: fully retreated state of ref. 2 under 1.8 °C ocean warming (red dashed line); maximum simulated MIS 5e retreat of ref. 3, equivalent to approximately 2 °C ocean and atmospheric warming (black dashed line); and modelled retreat of ref. 9 for both 2 °C ocean and atmospheric warming (ochre dotted line approximately following modern coastline) and 4 °C ocean and atmospheric warming (white dotted line). Labels C, N, and M indicate positions of Cook, Ninnis, and Mertz ice shelves, respectively.

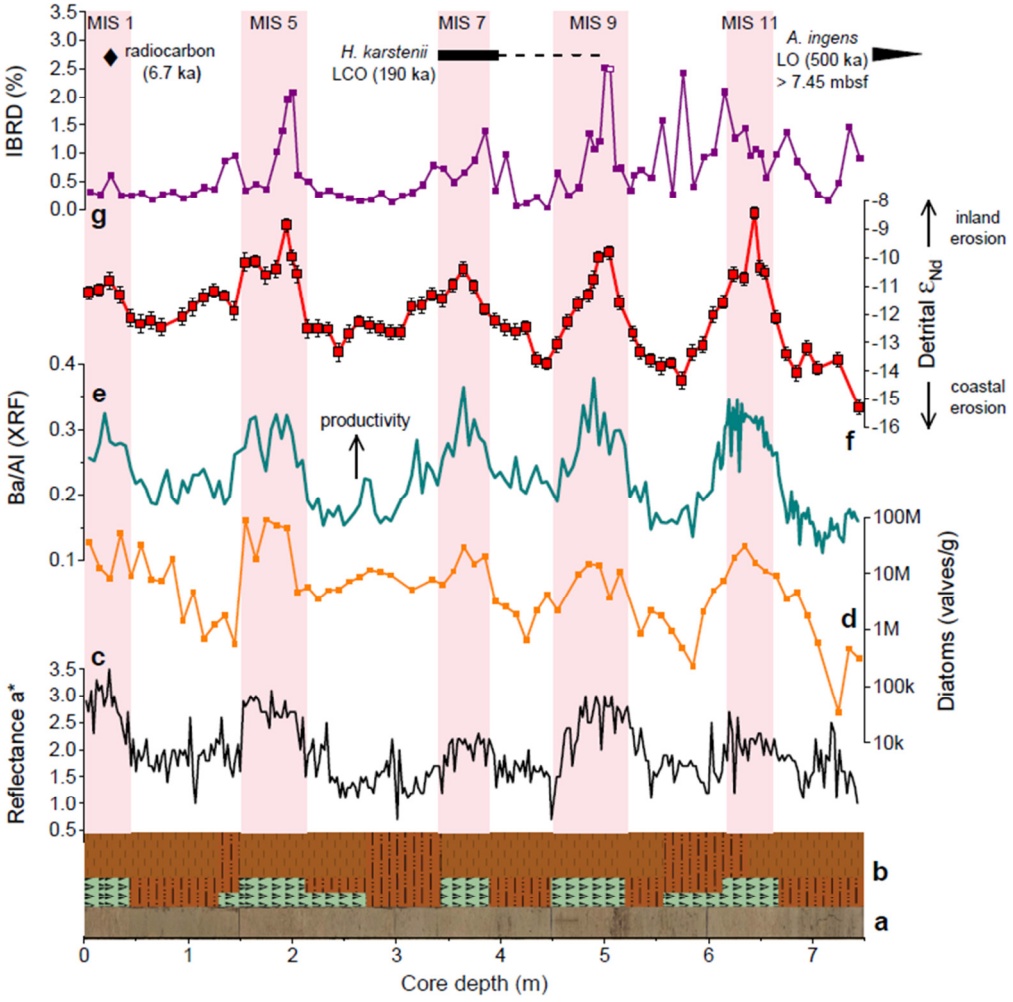

Figure 2: **Late Pleistocene records from core U1361A spanning MIS 1 to MIS 12**. (**a**) core images, (**b**) lithological log (green layers with 'V' symbol = diatom ooze; brown layers with long dashes = silty clay; brown layers with short dashes = bioturbated clay), (**c**) sediment reflectance (a*), (**d**) diatom abundance (logarithmic scale), (**e**) Ba/Al ratios (XRF-scanner counts), (**f**) detrital sediment Nd isotopes (arrows indicate coastal erosion of Lower Paleozoic granitoids versus inland erosion of FLIP/Beacon lithologies; error bars are 2 s.d. external reproducibility), (**g**) iceberg rafted debris (IBRD, % 250 µm – 2 mm; open square represents one data point that plots off the scale with 7.5 % IBRD at 5.05 m depth). Pink bars highlight interglacial periods, based on the dominance of diatom-rich clay. Marine isotope stage (MIS) numbers are labelled at the top, together with chronostratigraphic constraints (LCO = Last Common Occurrence, LO = Last Occurrence; Methods). Data in panels (a-c) from ref. 20; all other data from this study (Tables S1, S4-5, S7-8).

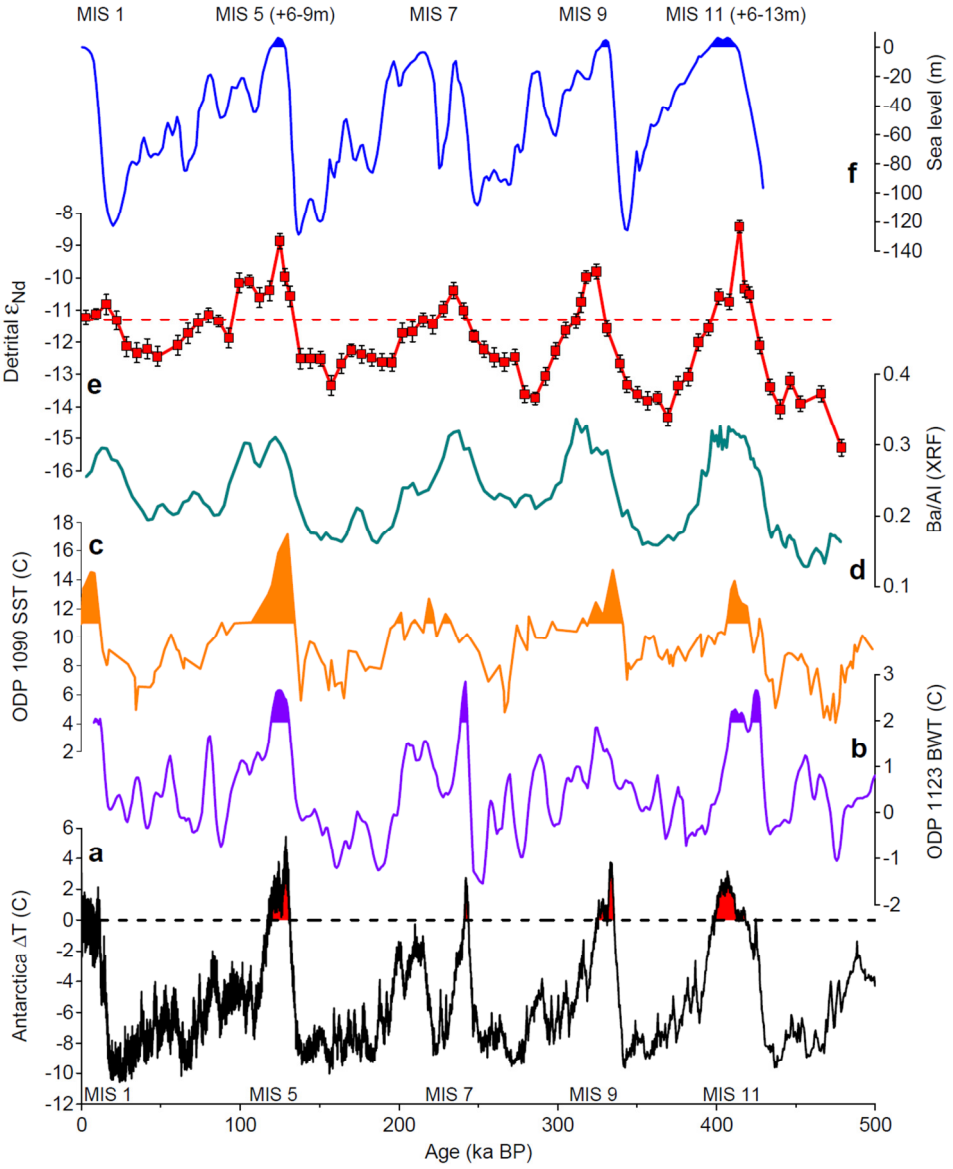

Figure 3: **Comparison of core U1361A records to regional paleoclimate and global sea level records**. (**a**) Antarctic ice core temperature difference (ΔT, difference from mean values of the last millennium) derived from deuterium isotopes (δD) at EPICA Dome C (ref. 11) plotted on EDC3 age scale, (**b**) Southern Ocean bottom water temperature (BWT) from Mg/Ca at ODP Site 1123 (ref. 18), (**c**) Southern Ocean sea surface temperature (SST) from alkenones at ODP Site 1090 (ref. 19), (**d**) Ba/Al ratios (XRF-scanner counts; 3-point smoothed) in U1361A, (**e**) bulk detrital sediment Nd isotopes in U1361A (error bars are 2 s.d. external reproducibility), (**f**) sea level proxy from benthic oxygen isotopes[28], labelled with MIS numbers and sea level estimates from MIS 5e and MIS 11 (ref. 17). Shading in panels (a-c, f) represents intervals with values above modern (or late Holocene core top), and the red dashed line in panel (e) indicates the core top ε_{Nd} value of U1361A. For chronostratigraphic constraints on U1361A, see Supplementary Table S8 and Methods.

Methods

Detrital sediment Nd isotope measurements. 75 samples from core U1361A were analysed for detrital sediment Nd isotopes (Supplementary Table S1), after leaching to remove any authigenic ferromanganese oxide phases[5,31-33]. Bulk samples of ~0.5-1 g were leached twice in an acid-reductive solution of hydroxylamine hydrochloride/acetic acid, including a second leach of at least 12 hours in 0.02 M hydroxylamine hydrochloride/25 % buffered acetic acid. After crushing and homogenisation, digestion of the detrital residue was carried out on a ~50 mg subsample by hotplate digestion[5] using a mixture of 2 ml 23 M HF, 1 ml 16 M HNO_3, and 0.6 ml 20 M $HClO_4$ (repeated twice), and then a mixture of 2 ml 23 M HF and 1 ml 16 M HNO_3. The rare earth element fraction was separated using either Eichrom TRU spec resin (100-120 μm mesh) or cation exchange resin (200-400 μm mesh), and the Nd fraction was isolated using Eichrom LN spec resin (50-100 μm mesh) on volumetrically calibrated Teflon columns. The approach followed ref. 5, with the replacement of TRU spec resin by cation exchange resin found to improve column yields.

Neodymium isotopic compositions were analysed on the Nu Plasma multi-collector inductively coupled plasma mass spectrometer (MC-ICP-MS) in the MAGIC laboratories at Imperial College London. Mass bias was corrected using the exponential law (to $^{146}Nd/^{144}Nd = 0.7219$). A correction for direct ^{144}Sm interference was also applied, with all samples significantly below the threshold determined for accurate correction (< 0.1 % of the ^{144}Nd signal). Sample measurements were bracketed by concentration-matched JNdi-1 Nd isotope standards and data from each analytical session were adjusted to give agreement with the literature value[34]. The external reproducibility was estimated from the within-session standard deviation (2 s.d.) on those standards. Over the course of analyses, measurements of

rock standard BCR-2 gave $^{143}Nd/^{144}Nd$ = 0.512640 ± 0.000016 (n = 31), in excellent agreement with literature values[35], and indicating a long term reproducibility of 0.31 epsilon units. Procedural and column blanks were typically 4 to 18 pg, and hence negligible.

Robustness of detrital sediment Nd isotope record. Unlike some other radiogenic isotope systems (e.g. Sr, Hf), Nd isotopes are relatively insensitive to grain size fractionation[36], making them a robust indicator of sediment provenance. However, if changes in sediment transport processes led to the supply of sediment from different sources, a link between grain size and Nd isotopes could emerge, which would complicate provenance interpretations. In order to test for any potential bias in our detrital Nd isotope record measured on the bulk sediment fraction, we additionally measured Nd isotopes on the fine-grained fraction (< 63 μm) for a subset of 10 samples, including both peak glacial and interglacial conditions (Supplementary Table S2). The fine fraction was separated by wet sieving and then subject to leaching, digestion, Nd separation and isotope measurement identically to the bulk sediment. Procedural blanks were 1.3 ng, representing less than 0.02 % of sample Nd and hence negligible, while all five full procedural replicates yielded Nd isotope results that agreed within error (Supplementary Table S2).

Since comparable glacial-interglacial Nd isotope changes are recorded in the < 63 μm fraction and the bulk fraction (Extended Data Fig. 1), it is clear that grain size (potentially linked to sediment transport) has an insignificant influence on the detrital Nd isotope record. In detail, two out of ten samples (from interglacials MIS 5 and MIS 11) show a small but resolvable offset of around 1 ε_{Nd} unit towards more radiogenic values in the bulk sediment than the fine fraction (Extended Data Fig. 1). This observation further constrains that the radiogenic Nd isotope signal from FLIP/Beacon lithologies is not restricted to a fine-grained silt or clay fraction but is also contained within sand-sized material that could be derived

from turbidity currents or ice-rafting. Given the potential of ocean currents to transport material only within the silt fraction[37], this evidence is consistent with a local source rather than a strengthened alongslope current in driving the radiogenic Nd isotope excursions.

A final indication that grain size and/or sediment transport are not major controls on the detrital Nd isotope record is given by the lack of a direct correlation between the IBRD record (% 250 μm – 2 mm fraction) and detrital Nd isotopes (Fig. 2). While there were generally IBRD peaks during deglaciation, the Nd isotope changes were often sustained throughout interglacials while IBRD was generally minimal or absent. Hence, the mechanism of sediment delivery appears to have been decoupled from the provenance information, which supports the complementary interpretation of IBRD as an indicator of dynamic processes (see below) and Nd isotopes as an indicator of the zone of glacial erosion. As previously shown in this region[38], provenance information from the bulk or fine sediment fraction is more useful as an indicator of glacial erosion than evidence from the IBRD fraction, hence our focus here on the former approach.

Supporting evidence on provenance changes from reductive sediment leachates. Acid-reductive sediment leaching is used to extract authigenic ferromanganese oxides or other reactive phases that are dispersed within a sediment core[31-33,39]. In many settings, this approach is useful for reconstructing past deep seawater compositions, but in certain cases it has been shown to yield compositions that reflect local sedimentary inputs, either through their partial dissolution during extraction[31] or through in-situ exchange with pore water[40]. Such a local influence is most likely at ocean margin sites where terrigenous-rich sediments may contain preformed ferromanganese oxides[41], or in locations where reactive volcanics are present in the sediment[31,40,42,43].

In this study, we analysed acid-reductive sediment leachates, based on the methods of both refs. 31 and 39, including 1 hour leaches (n = 18) and subsequent overnight leaches (n = 6) (Supplementary Table S3). During glacial periods, the leachate Nd isotopic compositions (ε_{Nd} = -5.6 to -10.5; Extended Data Fig. 1) are consistent with the range of possible compositions of Circumpolar Deep Water or Antarctic Bottom Water[44,45], although an influence of a mixed detrital component (Lower Paleozoic and FLIP/Beacon) on the recorded signature cannot be ruled out. However, during interglacial periods (particularly MIS 5, 9, and 11), the leachate compositions (ε_{Nd} = -3.2 to -6.1) are too radiogenic to reflect the composition of any likely local bottom water, but are instead consistent with a major influence from a reactive basaltic FLIP source (Extended Data Fig. 1). Therefore, the leachate data provide strong independent support for our provenance interpretations based on the detrital sediment Nd isotope record.

Detrital sediment Sr isotope measurements. Measurements of Sr isotopes were made on the same subset of 10 fine-grained sediment fractions (< 63 μm) that were analysed for Nd isotopes, spanning both peak glacial and interglacial conditions (Supplementary Table S2). Following rare earth element separation, samples were processed through Eichrom Sr-Spec resin (100 – 120 μm mesh) to isolate the Sr fraction. Strontium isotopes were analysed on the Thermo Scientific Triton thermal ionisation mass spectrometer (TIMS) in the MAGIC laboratories at Imperial College London. Samples were loaded onto degassed single tungsten filaments in 1 μl 6M HCl, followed by 1 μl of tantalum chloride activator. Measurements were made in static mode, with instrumental mass bias corrected using the exponential law (to $^{88}Sr/^{86}Sr = 8.375$), and interferences of ^{87}Rb corrected using an $^{87}Rb/^{85}Rb$ ratio of 0.3860. Long-term repeated analysis of the NBS 987 Sr standard in the MAGIC laboratories yielded $^{87}Sr/^{86}Sr = 0.710247 \pm 0.000019$ (2 s.d., n = 84) and reported $^{87}Sr/^{86}Sr$ ratios were corrected to the published value (0.710252 ± 0.000013; ref. 35). Ten separate digests of rock standard BCR-2 gave $^{87}Sr/^{86}Sr = 0.705010 \pm 0.000014$ (2 s.d., n = 42), in good agreement with the

published value (0.705013 ± 0.000010; ref. 35). The procedural blank associated with this sample set was ~6 ng, representing less than a 0.5 % contribution to sample measurements.

Stability of provenance endmembers from combined Nd-Sr isotopes. The combined Nd and Sr isotope dataset for the late Pleistocene is fully consistent with mixing between Lower Paleozoic and FLIP/Beacon lithologies, and also records an identical trend to Pliocene data from U1361 (Extended Data Fig. 2). We therefore infer similar provenance variations for both intervals, which additionally appears to indicate that any long term erosional changes (e.g. ref. 46) have not impacted on the regional bedrock sources available for erosion over this period of time.

IBRD measurements. 97 samples from core U1361A were processed for grain size analysis at Victoria University of Wellington to provide evidence on iceberg-rafted debris (IBRD) content (Supplementary Table S4). Dried samples were weighed and then wet-sieved to recover the coarse sand fraction (250 μm to 2 mm), which has previously been used to indicate IBRD in Arctic and Antarctic studies[6,47]. The > 250 μm fraction was dissolved of biogenic silica using 2M NaOH, and then dried and weighed to obtain a weight percent of IBRD fraction (250 μm to 2 mm) relative to the bulk sediment. Each sample was visually examined again under binocular microscope for volcanic ash layers, as well as for any authigenic minerals or biogenic components that could bias the IBRD weights, and such components were manually removed if present. For this study, we did not calculate IBRD mass accumulation rates, but they would scale almost directly with the weight percent IBRD (since our age model assumes constant sedimentation rates and there are no large shifts or trends in dry bulk density in this interval).

Interpretation of IBRD record. Antarctica currently loses approximately half of its ice mass via iceberg calving[48], while distinct pulses of IBRD observed in the Scotia Sea region during

the last deglaciation have been interpreted as representing collapse of the marine-based sector of the WAIS[49]. Site U1361 is located in the pathway of the Antarctic Coastal Current which transports icebergs into the region in a predictable manner, as opposed to regions further north or east[50]. Furthermore, it is located south of the present southern boundary of the Antarctic Circumpolar Current (ACC), in a region dominated by geostrophic and bathymetrically controlled currents. Since the southern boundary front of the ACC is bathymetrically controlled by the continental rise on which Site U1361 is located, changes in ocean currents or sea surface temperature are unlikely to have contributed significantly to changes recorded in our IBRD record. Site U1361 is also a suitable site for this proxy because it is proximal to outlet glaciers of the Antarctic margin, such that smaller icebergs with basal debris could survive moderate levels of sea surface warming (even to the elevated temperatures inferred for the Pliocene[5,6]), but also not so close to the continent as to be influenced by a single outlet glacier or a single iceberg dumping[50].

Studies from the Pliocene interval of U1361 indicate that the IBRD record contains a statistically-significant, high fidelity orbital signal, confirming that iceberg calving is not a random process at this site[6]. As in that study, we interpret the new IBRD record (Fig. 2) as primarily representing changes in the dynamic discharge of outlet glaciers and ice streams, likely occurring during periods of enhanced glacial retreat. One potential complicating factor in the interpretation of this record is that the development of large ice shelves during glacial maxima and minima could theoretically result in tabular icebergs that lack basal debris, such as for the modern Mertz Glacier tongue or the Ross Ice Shelf. In this scenario, our IBRD record (Fig. 2) may only document the calving of smaller icebergs from outlet glaciers, such that the absence of IBRD during the glacials could indicate the presence of stabilising ice shelf systems prior to retreat in the Wilkes Subglacial Basin, and the relative lack of IBRD during interglacials could reflect the formation of large ice shelves within a deglaciated

embayment. However, this scenario would still imply a shift in glacial dynamics and ice sheet extent through a glacial cycle, which is supported by the Nd isotope evidence that pulses in IBRD were associated with major switches in erosional sources (Fig. 2). Further considerations regarding the IBRD proxy at this site are discussed in detail by refs. 6,51.

Sortable silt measurements. Sortable silt analysis was carried out on 75 samples using the method outlined in ref. 52 and reported as the mean grain size of the 10-63 μm detrital fraction (Table S4). Carbonate and biogenic silica were removed from sediment samples by reacting with 1 M acetic acid for 24 hours, followed by heating to 85 °C in 2 M sodium carbonate for 5 hours, with samples being agitated several times during each step. Samples were then suspended in 0.2 % sodium hexametaphosphate solution and placed on a rotating wheel before analysis using a Beckman Multisizer 3 Coulter Counter at the University of Queensland. Repeated analysis was performed on a subset of samples in an arbitrary order over several days and average standard deviation of replicate analysis was ±0.1 μm.

Sedimentological constraints on sediment transport. Our sortable silt record indicates a very fine grain size (13.5 μm), at the low end of the proxy range, and a lack of variation through time (1 s.d. = 0.5 μm) (Table S4). While this result is suggestive of a low current speed, we caution that there are caveats in applying the sortable silt method in a setting influenced by turbidity currents and IBRD, and that this proxy cannot provide a quantitative estimate of current speed[53]. Nevertheless, the lack of correlation between sortable silt grain size and detrital Nd isotopes provides no evidence to suggest a control on our provenance record by current transport. In this context, it is important to emphasise that Site U1361 was cored on a turbidite levee deposit[20]. From both its geometry[20] and seafloor bedforms[54], it is unambiguous that the majority of sediment supplied to the site is derived from the adjacent Jussieau Canyon system, which itself is fed by sediment from the adjacent continental shelf.

The lack of variation in the sortable silt grain size record is consistent with such a setting. Given the proximity to such local sediment inputs, and with regional dust inputs at the East Antarctic margin being among the lowest in the world[55], we also rule out any possible control of dust supply on sediment provenance at Site U1361.

Measurement of Ba/Al ratios. Bulk major element compositions were measured using an Avaatech X-ray fluorescence (XRF) core scanner at the IODP Gulf Coast Repository at Texas A & M University (USA) during March 2011. Non-destructive XRF core scanning was performed at 10 kV in order to measure the relative content of elements including aluminium (Al), iron (Fe), and barium (Ba). Measurements were made continuously at every 5 cm down core from sections U1361A-1H-1 to U1361A-1H-5, over a 1.2 cm^2 area, with a slit size of 10 mm, a current of 0.8 mA, and a sampling time of 45 s. The Ba and Al counts, and the Ba/Al count ratio, are reported here (Supplementary Table S5).

Interpretation and principal component analysis of Ba/Al ratios. Barium-based proxies (e.g. Ba/Al ratios) in pelagic sediments have variously been interpreted as a marine productivity proxy[56,57], as a meltwater tracer[58], or as an indicator of intense bottom currents[59], among other processes[60]. In order to interpret the Ba/Al ratio at Site U1361, we applied principal component analysis (PCA)[59] to the data from the upper 7 mbsf of the core. The PCA analysis yielded two significant components (Supplementary Table S6). The first principal component (PC1) describes 31.4 % of the total variance, with main negative loadings for Ca and Mn, and positive loadings for all other elements (except K). This variable could represent a link between Mn and Ca enrichment peaks during glacial to interglacial transitions, which is the focus of ongoing research. The second principal component (PC2) describes 26.2 % of the variance, with positive loadings for Ca, Ba, S, and Si (in descending order), and negative loadings for Fe, Al, K, Mn, and Ti. Such a relationship between the

loadings for PC2 is characteristic of biogenic components in the positive axis and aluminosilicates in the negative axis[61].

Visual inspections suggest that Si and Ca enrichment are related to sediments rich in diatoms (Si) and coccoliths (Ca). Because Ba is related positively to Ca, Si, and S for PC2, we conclude that Ba is related to marine productivity and is probably present in the form of biogenic barite ($BaSO_4$), while normalisation to a detrital immobile element (e.g. Al) corrects for dilution effects[62]. Through time, loadings of PC2 are virtually parallel to the Ba/Al ratio (Supplementary Table S6), with both showing regular alternations coincident with glacial-interglacial cycles. Based on these correlations, and previous studies at this site[5,51], we conclude that the Ba/Al ratio is a robust productivity proxy at U1361.

Diatom counts. Quantitative diatom slides were prepared following a method modified from ref. 63 for 70 samples between 0.05 and 7.45 mbsf at ~10 cm intervals. For each sample, a uniform mass of 0.50 mg raw sediment was digested in 15 ml 30 % hydrogen peroxide with 5 ml sodium hexametaphosphate for one hour in a 60° C water bath, to remove organic material and aid disaggregation. Samples were then triple-rinsed by centrifuging at 1600 rpm for 7 minutes, decanting, and topping up with distilled water. After the final rinse, samples were re-suspended, poured into a beaker that was topped up to 100 ml with distilled water, and stirred to homogenise. 300 µl of homogenised solution was pipetted onto a 22 x 38 mm cover slip placed at the bottom of a glass petri dish, and again topped up with distilled water. Each dish was fitted with a cotton string for wicking and allowed to settle and dry for 48 hours, after which the dry cover slips were mounted to glass slides using Norland Optical Adhesive #61 (refractive index of 1.56) and cured under UV light for 30 mins.

Three slides were prepared for each sample and examined microscopically. Where possible, 250-300 valves were counted for each slide to yield statistically robust assemblage data.

Where total valve counts were lower, at least 35 fields of view were evaluated for each slide to determine absolute diatom abundance (ADA). For each sample, triplicate counts were combined to produce a single data set (Supplementary Table S7). ADA was calculated from a measured field of view of 3.14 mm^2 and a total settling area of 6361.72 mm^2. Diatoms were identified to the species level, following the same taxonomic concepts used during IODP Exp. 318 (ref. 20).

Age control. A Holocene age for the upper portion of U1361A is confirmed by a single radiocarbon date from 0.25-0.27 mbsf (Supplementary Table S8). The radiocarbon analysis was performed on the bulk organic fraction at Beta Analytic. The sample was sieved at 180 μm and pretreated with acid washes to remove carbonate. Conventional ^{14}C ages were calculated according to ref. 64 using a $\delta^{13}C$ correction for isotopic fractionation. A marine reservoir correction of 1300 years was applied[65] and the ^{14}C age was calibrated using the Marine 13 calibration curve[66].

Additional age control for the late Pleistocene interval is provided by the well-established last common occurrence of the diatom *Hemidiscus karstenii* at 190 ka BP (kyr before present; refs. 67,68), which is identified at 3.45 mbsf (Supplementary Tables S7 and S8; Extended Data Fig. 3). Immediately below our interval of focus, we identify two paleomagnetic reversals and two additional diatom last occurrences that further constrain the age of our sequence (Supplementary Table S8; Extended Data Fig. 3). The upper depth constraint for chron C1n (11.19 mbsf) has been revised from ref. 69 based on magnetostratigraphy of the U1361 composite splice (U1361A and U1361B; ref. 20). To more precisely constrain the core depths of last occurrences of *Actinocyclus ingens* and *Thalassiosira fasciculata*[70], additional samples from U1361A core 2H were examined following the Expedition 318 shipboard methodology for diatom biostratigraphy[20]. These secondary constraints confirm

that the base of our record is younger than 500 ka and support our assignment of peaks in multiple proxies to interglacial marine isotope stages 1-11 (Extended Data Fig. 3).

Methods references

31 Wilson, D. J., Piotrowski, A. M., Galy, A. & Clegg, J. A. Reactivity of neodymium carriers in deep sea sediments: Implications for boundary exchange and paleoceanography. *Geochim. Cosmochim. Acta* **109**, 197-221 (2013).

32 Bayon, G. *et al.* An improved method for extracting marine sediment fractions and its application to Sr and Nd isotopic analysis. *Chemical Geology* **187**, 179-199 (2002).

33 Chester, R. & Hughes, M. J. A chemical technique for the separation of ferro-manganese minerals, carbonate minerals and adsorbed trace elements from pelagic sediments. *Chemical Geology* **2**, 249-262 (1967).

34 Tanaka, T. *et al.* JNdi-1: a neodymium isotopic reference in consistency with LaJolla neodymium. *Chemical Geology* **168**, 279-281 (2000).

35 Weis, D. *et al.* High-precision isotopic characterization of USGS reference materials by TIMS and MC-ICP-MS. *Geochem. Geophys. Geosyst.* **7**, doi: 10.1029/2006gc001283 (2006).

36 Eisenhauer, A. *et al.* Grain size separation and sediment mixing in Arctic Ocean sediments: evidence from the strontium isotope systematic. *Chemical Geology* **158**, 173-188 (1999).

37 Maggi, F. The settling velocity of mineral, biomineral, and biological particles and aggregates in water. *J. Geophys. Res.-Oceans* **118**, 2118-2132 (2013).

38 Cook, C. P. *et al.* Glacial erosion of East Antarctica in the Pliocene: A comparative study of multiple marine sediment provenance tracers. *Chemical Geology* **466**, 199-218 (2017).

39 Chen, T. Y., Frank, M., Haley, B. A., Gutjahr, M. & Spielhagen, R. F. Variations of North Atlantic inflow to the central Arctic Ocean over the last 14 million years inferred from hafnium and neodymium isotopes. *Earth Planet. Sci. Lett.* **353**, 82-92 (2012).

40 Du, J. H., Haley, B. A. & Mix, A. C. Neodymium isotopes in authigenic phases, bottom waters and detrital sediments in the Gulf of Alaska and their implications for paleo-circulation reconstruction. *Geochim. Cosmochim. Acta* **193**, 14-35 (2016).

41 Bayon, G., German, C. R., Burton, K. W., Nesbitt, R. W. & Rogers, N. Sedimentary Fe-Mn oxyhydroxides as paleoceanographic archives and the role of aeolian flux in regulating oceanic dissolved REE. *Earth Planet. Sci. Lett.* **224**, 477-492 (2004).

42 Blaser, P. *et al.* Extracting foraminiferal seawater Nd isotope signatures from bulk deep sea sediment by chemical leaching. *Chemical Geology* **439**, 189-204 (2016).

43 Elmore, A. C., Piotrowski, A. M., Wright, J. D. & Scrivner, A. E. Testing the extraction of past seawater Nd isotopic composition from North Atlantic deep sea sediments and foraminifera. *Geochem. Geophys. Geosyst.* **12**, doi: 10.1029/2011gc003741 (2011).

44 van de Flierdt, T. *et al.* Neodymium in the oceans: a global database, a regional comparison and implications for palaeoceanographic research. *Philosophical Transactions of the Royal Society a-Mathematical Physical and Engineering Sciences* **374**, doi: 10.1098/rsta.2015.0293 (2016).

45 Skinner, L. C. *et al.* North Atlantic versus Southern Ocean contributions to a deglacial surge in deep ocean ventilation. *Geology* **41**, 667-670 (2013).

46 Frederick, B. C. *et al.* Distribution of subglacial sediments across the Wilkes Subglacial Basin, East Antarctica. *J. Geophys. Res.-Earth Surf.* **121**, 790-813 (2016).

47 Krissek, L. A. in *Proc. ODP, Sci. Results, 145* (eds D.K. Rea, I.A. Basov, D.W. Scholl, & J.F. Allan) 179-194 (Ocean Drilling Program, 1995).

48 Depoorter, M. A. *et al.* Calving fluxes and basal melt rates of Antarctic ice shelves. *Nature* **502**, 89-92 (2013).

49 Weber, M. E. *et al.* Millennial-scale variability in Antarctic ice-sheet discharge during the last deglaciation. *Nature* **510**, 134-138 (2014).

50 Stuart, K. M. & Long, D. G. Tracking large tabular icebergs using the SeaWinds Ku-band microwave scatterometer. *Deep-Sea Res. Part II-Top. Stud. Oceanogr.* **58**, 1285-1300 (2011).

51 Bertram, R. A. *et al.* Pliocene deglacial event timelines and the biogeochemical response offshore Wilkes Subglacial Basin, East Antarctica. *Earth Planet. Sci. Lett.* **494**, 109-116 (2018).

52 McCave, I. N. Sedimentary processes and the creation of the stratigraphic record in the Late Quaternary North Atlantic Ocean. *Philos. Trans. R. Soc. Lond. Ser. B-Biol. Sci.* **348**, 229-240 (1995).

53 McCave, I. N. & Hall, I. R. Size sorting in marine muds: Processes, pitfalls, and prospects for paleoflow-speed proxies. *Geochem. Geophys. Geosyst.* **7**, doi: 10.1029/2006GC001284 (2006).

54 Donda, F., Brancolini, G., De Santis, L. & Trincardi, F. Seismic facies and sedimentary processes on the continental rise off Wilkes Land (East Antarctica): evidence of bottom current activity. *Deep-Sea Res. Part II-Top. Stud. Oceanogr.* **50**, 1509-1527 (2003).

55 Mahowald, N., Albani, S., Engelstaedter, S., Winckler, G. & Goman, M. Model insight into glacial-interglacial paleodust records. *Quat. Sci. Rev.* **30**, 832-854 (2011).

56 Jimenez-Espejo, F. J. *et al.* Detrital input, productivity fluctuations, and water mass circulation in the westernmost Mediterranean Sea since the Last Glacial Maximum. *Geochem. Geophys. Geosyst.* **9**, doi: 10.1029/2008GC002096 (2008).

57 Bonn, W. J., Gingele, F. X., Grobe, H., Mackensen, A. & Futterer, D. K. Palaeoproductivity at the Antarctic continental margin: opal and barium records for the last 400 ka. *Paleogeogr. Paleoclimatol. Paleoecol.* **139**, 195-211 (1998).

58 Plewa, K., Meggers, H. & Kasten, S. Barium in sediments off northwest Africa: A tracer for paleoproductivity or meltwater events? *Paleoceanography* **21**, doi: 10.1029/2005PA001136 (2006).

59 Bahr, A. *et al.* Deciphering bottom current velocity and paleoclimate signals from contourite deposits in the Gulf of Cadiz during the last 140 kyr: An inorganic geochemical approach. *Geochem. Geophys. Geosyst.* **15**, 3145-3160 (2014).

60 Griffith, E. M. & Paytan, A. Barite in the ocean - occurrence, geochemistry and palaeoceanographic applications. *Sedimentology* **59**, 1817-1835 (2012).

61 van den Berg, B. C. J. *et al.* Astronomical tuning for the upper Messinian Spanish Atlantic margin: Disentangling basin evolution, climate cyclicity and MOW. *Glob. Planet. Change* **135**, 89-103 (2015).

62 Van der Weijden, C. H. Pitfalls of normalization of marine geochemical data using a common divisor. *Mar. Geol.* **184**, 167-187 (2002).

63 Rathburn, A. E., Pichon, J. J., Ayress, M. A. & DeDeckker, P. Microfossil and stable-isotope evidence for changes in Late Holocene palaeoproductivity and palaeoceanographic conditions in the Prydz Bay region of Antarctica. *Paleogeogr. Paleoclimatol. Paleoecol.* **131**, 485-510 (1997).

64 Stuiver, M. & Polach, H. A. Discussion: reporting of ^{14}C data. *Radiocarbon* **19**, 355-363 (1977).

65 Ingolfsson, O. *et al.* Antarctic glacial history since the Last Glacial Maximum: an overview of the record on land. *Antarct. Sci.* **10**, 326-344 (1998).

66 Reimer, P. J. *et al.* IntCal13 and Marine13 radiocarbon age calibration curves 0-50,000 years cal BP. *Radiocarbon* **55**, 1869-1887 (2013).

67 Presti, M. *et al.* Sediment delivery and depositional patterns off Adelie Land (East Antarctica) in relation to late Quaternary climatic cycles. *Mar. Geol.* **284**, 96-113 (2011).

68 Gersonde, R. & Barcena, M. A. Revision of the upper Pliocene - Pleistocene diatom biostratigraphy for the northern belt of the Southern Ocean. *Micropaleontology* **44**, 84-98 (1998).

69 Tauxe, L. *et al.* Chronostratigraphic framework for the IODP Expedition 318 cores from the Wilkes Land Margin: Constraints for paleoceanographic reconstruction. *Paleoceanography* **27**, doi: 10.1029/2012pa002308 (2012).

70 Cody, R. *et al.* Selection and stability of quantitative stratigraphic age models: Plio-Pleistocene glaciomarine sediments in the ANDRILL 1B drillcore, McMurdo Ice Shelf. *Glob. Planet. Change* **96-97**, 143-156 (2012).

71 Lisiecki, L. E. & Raymo, M. E. A Pliocene-Pleistocene stack of 57 globally distributed benthic $\delta^{18}O$ records. *Paleoceanography* **20**, doi: 10.1029/2004pa001071 (2005).

Extended Data Figures

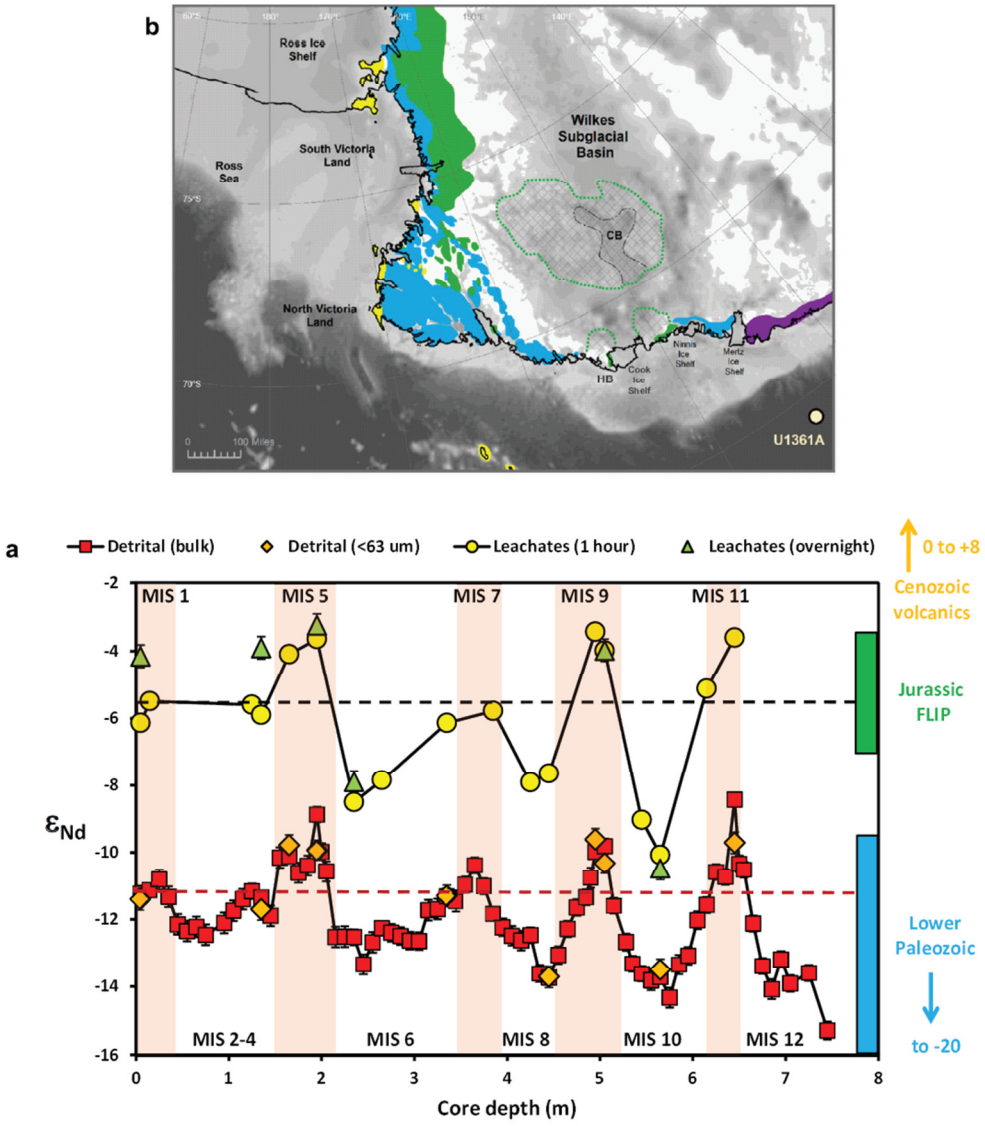

Extended Data Figure 1: Neodymium isotope data for bulk detrital sediment, < 63 μm fraction, and reductive sediment leachates in U1361A, in comparison to regional bedrock endmembers. (**a**) Down core measurements on the different fractions, with boxes and arrows on the right indicating bedrock endmember compositions in the region (refs. 5,38 and refs. therein). Horizontal lines indicate Holocene core top values for bulk detrital samples (red dashed line) and 1 hour leachate samples (black dashed line). Error bars are 2 s.d. external reproducibility, and are smaller than the symbol sizes where not shown. (**b**) Regional bedrock map, with those same bedrock endmembers located by coloured shading (map redrawn from ref. 5, with topography from ref. 12, and the subglacial extent of the FLIP shown by a green dotted outline inferred from ref. 21). In addition to the three endmembers shown in (a), purple shading on the map indicates Archaean to Proterozoic basement rocks of the Adélie Craton, with highly unradiogenic Nd isotopic compositions (ε_{Nd} = -20 to -29). CB = Central Basin, HB = Horn Bluff. For interpretation of the leachate and detrital Nd isotope data, see Methods.

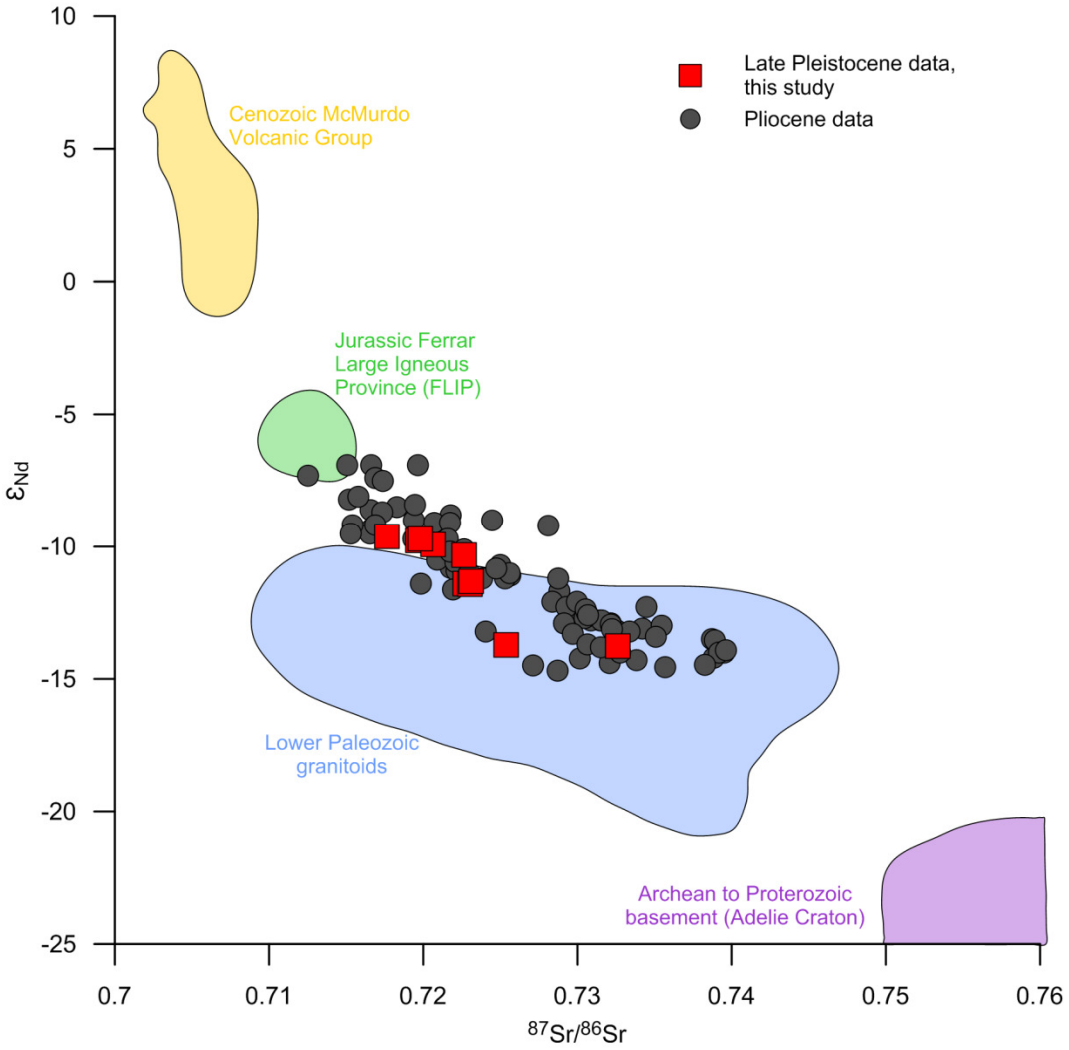

Extended Data Figure 2: Neodymium isotope versus Sr isotope crossplot for late Pleistocene fine fraction (< 63 μm) sediments in U1361A, in comparison to Pliocene detrital sediments from Site U1361 and regional bedrock endmembers. The Pliocene data are based on either the < 63 μm or < 150 μm size fractions[5,38,51], while bedrock endmember compositions are based on refs. 5,38 (and refs. therein). These data indicate identical trends between the Pliocene and Pleistocene, from which we infer similar provenance variations during both these intervals.

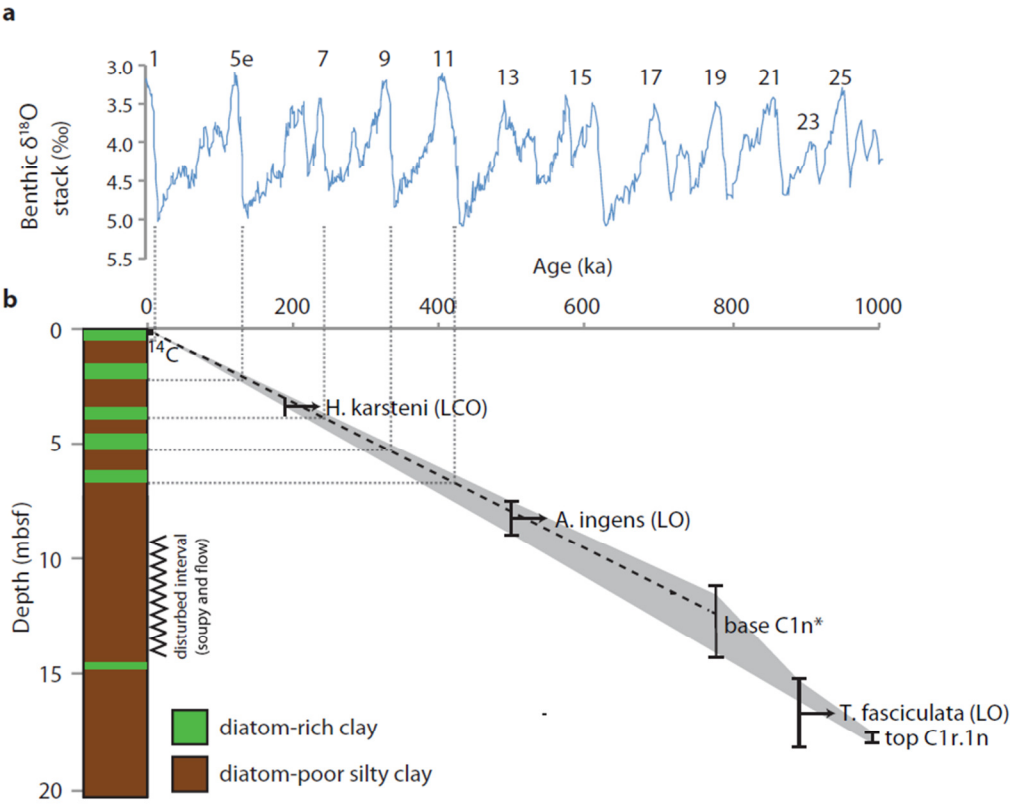

Extended Data Figure 3: Age model for U1361A. (**a**) LR04 benthic oxygen isotope ($\delta^{18}O$) stack[71], labelled with interglacial MIS numbers. (**b**) Age/depth constraints for U1361A cores 1H and 2H, plotted alongside lithology. Vertical bars for each datum indicate upper and lower depth constraints in U1361A (Supplementary Table S8). Black dashed line is a linear model fit through the Holocene radiocarbon age, *H. karsteni* last common occurrence (LCO), *A. ingens* last occurrence (LO) (upper and lower depths), and the base of chron C1n (*upper depth only, based on the splice to U1361B) (Supplementary Table S8). Forced to an intercept of 0 ka at 0 mbsf, this trendline produces the age/depth equation $y = 64.314x$, where y = age (ka) and x = depth (mbsf). This equation was used to calculate ages for Fig. 3 (panels d-e). Grey dotted lines tie lithological transitions to MIS boundaries, based on our age/depth constraints. Note that the Pleistocene section of the core below MIS 12 is affected by sediment disturbance, with extreme disturbance from 9.0-11.67 mbsf (soupy) and 11.67-14.26 mbsf (flow) represented schematically with a zigzag line. We have therefore restricted our provenance study to the upper ~7.5 mbsf.